

Convolution Based Techniques for Computing Self Attraction and Loading in MOM6

Anthony Chen¹, He Wang^{2,3,4}, Brian K. Arbic^{2,5}, and Robert Krasny¹

¹Department of Mathematics, University of Michigan, Ann Arbor, MI, USA

²Department of Earth and Environmental Sciences, University of Michigan, Ann Arbor, MI, USA

³UCAR, Boulder, CO, USA

⁴NOAA-GFDL, Princeton, NJ, USA

⁵Research School of Earth Sciences, Australian National University, Canberra, ACT, Australia

Correspondence: Anthony Chen (cygnari@umich.edu)

Abstract. Self Attraction and Loading (SAL), which includes the deformation of the solid Earth under the load of the ocean tide and the self-gravitation of the so-deformed Earth as well as of the ocean tides themselves, is an important term to include in numerical models of the ocean tides. Computing SAL is a challenging problem that is usually tackled using spherical harmonics. The spherical harmonic approach has several drawbacks which limit its accuracy. In this work, we propose an alternative technique based on a spherical convolution. We implement the convolution technique in the Modular Ocean Model, version 6, and demonstrate that it allows for more accurate tides when measured against tidal datasets based upon satellite altimetry. The convolution based SAL reduces the error by reducing spurious oscillations associated with the Gibbs phenomenon. These oscillations are large in coastal regions under the traditional spherical harmonic approach.

1 Introduction

Tides are an important component of the Earth system. In many open-ocean and coastal regions, tides are a critical component of sea level and current variability. Tides are also implicated as a major component of the ocean mixing cycle, which contributes significantly to the background oceanic stratification in both the coastal and pelagic ocean (Simpson and Hunter (1974); Munk and Wunsch (1998)). Tides are a result of astronomical gravitational forcing, and this tidal forcing drives periodic changes in the sea surface height (SSH) and in the currents. An improved understanding of the tides is important for deepening our understanding of the oceans and developing improved models.

Historically, tides were independently modeled from the rest of the ocean, primarily in barotropic tide models, which improved with increased computing power and data assimilation from satellite altimetry (Egbert et al. (1994); Le Provost et al. (1994); Parke and Hendershott (1980); Ray (1993); Schwiderski (1979); Shum et al. (1997); Stammer et al. (2014)). However, baroclinic models have historically excluded incorporating the tides. The first studies of tides in a baroclinic model were performed in a regional configuration (Cummins and Oey (1997); Kang et al. (2002); Merrifield et al. (2001)). In the past two decades, as computers have improved, tides have been explicitly incorporated into ocean general circulation models (Arbic (2022); Arbic et al. (2010); Müller et al. (2010); Schiller and Fiedler (2007); Thomas et al. (2001); Waterhouse et al. (2014)).

Running such models with combined tidal and atmospheric forcing at high spatial resolution allows for large scale investigations of the interactions of barotropic and internal tides with smaller scale oceanic phenomena, such as mesoscale eddies, and other components of the Earth system including the cryosphere.

An important effect to capture when modeling the tides is Self Attraction and Loading (SAL). This encompasses the physical effects of the self gravitation of the oceanic tidal elevations, the elastic response of the Earth's crust to the loading of the ocean tide, and resulting changes in the Earth's gravitational potential due to the self gravitation of the deformed solid Earth (Hendershott (1972)). SAL has large effects on the tides, changing the amplitude by up to 20% and impacting the phase significantly as well (Gordeev et al. (1977)). A simple approach to computing SAL in models uses the so-called scalar approximation (Accad and Pekeris (1978); Ray (1998)), in which the SAL is approximated as a constant multiplied by the tidal elevation. The scalar approximation, while simple and computationally efficient, is, however, less accurate than a fuller treatment using spherical harmonics, which properly account for the different responses of the ocean and solid Earth to harmonics of different scales. Early attempts to use the spherical harmonic SAL inline in models, as they are running, were computationally expensive (Stepanov and Hughes (2004)). This is because SAL is inherently a global calculation, in contrast to other terms in the momentum equations of numerical ocean models. More recent work, aided by improvements in computational power, have still focused on the use of spherical harmonics to compute SAL inline (Barton et al. (2022); Brus et al. (2023); Wang et al. (2024)).

In this work, we present an alternative to the spherical harmonic computation, based on the computation of a convolution with a SAL Green's function. There are a number of limitations to the spherical harmonic based SAL, including limitations on accuracy and the fact that spherical harmonics, being a global quantity, cannot easily be used in regional models. The convolution based SAL offers an alternative that could be incorporated into regional models in the future, and that offers improvements in the accuracy of the computed SAL, as we will show later. Sec. 2 describes our convolution based SAL. Sec. 3 describes the model configuration we use to test the convolution SAL, and Sec. 4 describes the results of our simulations, with a special emphasis on tidal errors and computational efficiencies using the convolution and spherical harmonic approaches.

2 Methods and Implementation

The Modular Ocean Model, version 6 (MOM6, Adcroft et al. (2019)), is a widely used open source numerical ocean general circulation model. The model is hydrostatic, and solves either a Boussinesq or non-Boussinesq equation set. For this paper, we use the model in a single layer configuration, in which case the equations for the dynamics reduce to the shallow water equations:

$$\frac{\partial \mathbf{u}}{\partial t} + (\mathbf{u} \cdot \nabla) \mathbf{u} + \mathbf{f} \times \mathbf{u} = -g \nabla \eta + \mathcal{F}, \quad (1)$$

$$\frac{\partial \eta}{\partial t} + \nabla \cdot (h \mathbf{u}) = 0, \quad (2)$$

where t is time, \mathbf{u} is the horizontal fluid velocity, $\mathbf{f} = f \mathbf{e}_r$, where f is the Coriolis parameter and \mathbf{e}_r is the radial outwards unit vector, η is the sea surface height, g is acceleration due to gravity, \mathcal{F} are other forces (for instance, friction), and h is the total

water column thickness. If the ocean floor has height $b(\mathbf{x})$, then h and η are related as $\eta(t, \mathbf{x}) = h(t, \mathbf{x}) + b(\mathbf{x})$. Eq. 1 describes the balance of momentum, and Eq. 2 describes the conservation of mass. For multi-layer configurations, this equation set can be supplemented with thermodynamic equations. The equation set is often replaced by the more general Boussinesq or non-Boussinesq equations in the multi-layer case. The horizontal discretization is based on the Arakawa C-grid . The horizontal grid is based on a global tripolar discretization with an Arakawa C-grid.

For this work, we include tidal forcing, SAL, wave drag, quadratic bottom boundary layer drag, and horizontal viscosity. Thus, our \mathcal{F} takes the form

$$\mathcal{F} = g\nabla(\eta_{\text{EQ}} + \eta_{\text{SAL}}) + \mathbf{F}_{\text{wave}} + \mathbf{F}_{\text{quad}} + \mathbf{F}_h, \quad (3)$$

where η_{EQ} is the equilibrium tidal forcing, η_{SAL} is the forcing due to SAL, \mathbf{F}_{wave} is parametrized linear wave drag, \mathbf{F}_{quad} is quadratic bottom drag, and \mathbf{F}_h is horizontal viscosity. The linear wave drag includes a non-dimensional tunable parameter χ . Further details on the wave drag scheme are given in Jayne and St. Laurent (2001) and Buijsman et al. (2015). The gradient of the SAL term has two components. We can write the SAL acceleration as

$$g\nabla\eta_{\text{SAL}} = \frac{g}{R_E} \frac{\partial\eta_{\text{SAL}}}{\partial\theta} \mathbf{e}_\theta + \frac{g}{R_E \cos\theta} \frac{\partial\eta_{\text{SAL}}}{\partial\phi} \mathbf{e}_\phi \quad (4)$$

where θ is the latitude, ϕ is the longitude, \mathbf{e}_θ is the unit vector in the latitudinal direction, \mathbf{e}_ϕ is the unit vector in the longitudinal direction, and R_E is the radius of the Earth. The coefficient of \mathbf{e}_ϕ is then the zonal acceleration, and the coefficient of \mathbf{e}_θ is the meridional acceleration.

2.1 Spherical Harmonics for Computing SAL

Recent efforts in computing SAL (Barton et al. (2022); Brus et al. (2023); Wang et al. (2024)) have used the spherical harmonic transform in line. If the sea surface height η has spherical harmonic components $\widehat{\eta}_{n,m}$, then the SAL potential is given as

$$\eta_{\text{SAL}}(\theta, \phi) = \sum_{n=0}^{\infty} \sum_{m=-n}^n \frac{3\rho_w(1+k'_n - h'_n)}{\rho_e(2n+1)} \widehat{\eta}_{n,m} Y_n^m(\theta, \phi), \quad (5)$$

where Y_n^m is the degree n order m spherical harmonic, ρ_w is the average density of seawater in kilograms per cubic meter, ρ_e is the average density of the Earth in kilograms per cubic meter, and k'_n and h'_n are the modified Load Love Numbers (LLNs), as discussed in Farrell (1972). Typical values we use for a single layer model configuration are a seawater density $\rho_w = 1035 \text{ kg m}^{-3}$ and an Earth density of $\rho_e = 5517 \text{ kg m}^{-3}$. When used in a multi-layer model, the sea surface height is replaced with the bottom pressure anomaly, and corresponding adjustments are made to the coefficients. In practice, the sum is truncated, usually going up to $n = 40$ (Brus et al. (2023)). For computing the $\widehat{\eta}_{n,m}$, two main approaches are used. The first is to employ a fast spherical harmonic transform (Barton et al. (2022)), but this faces challenges with parallel scaling. Additionally, on grids that are not latitude longitude grids, there are additional interpolation steps needed. The second is to directly compute the integrals

$$\widehat{\eta}_{n,m} = \int_0^{2\pi} \int_0^\pi Y_n^m(\theta, \phi) \eta(\theta, \phi) \sin\theta d\theta d\phi, \quad (6)$$

where Y_n^m is the degree n order m spherical harmonic (Brus et al. (2023); Wang et al. (2024)). This approach is better suited for parallelization, but can be prone to aliasing. Additionally, this spherical harmonic technique is susceptible to the Gibbs phenomenon near coastlines. The Gibbs phenomenon is a numerical effect that occurs when using Fourier series to approximate discontinuous functions. A finite truncation of the Fourier series near a discontinuity in the function being approximated will result in oscillatory errors, overshooting and undershooting the function. These errors do not decrease in magnitude as the number of Fourier components increases.

2.2 The Gibbs Phenomenon

The Gibbs phenomenon is a type of oscillatory error that occurs when working with the Fourier series of a function with a jump discontinuity (Gottlieb and Shu (1997)). Let g be a periodic function with period L and a jump discontinuity at a point x_0 with a limit from the left of $f(x_0^-)$ and a limit from the right of $f(x_0^+)$. Then, for any finite truncation of the Fourier series of g , at the point x_0 , the Fourier series will converge to $1/2(f(x_0^-) + f(x_0^+))$, but on both sides of the jump discontinuity, there will be an overshoot of approximately 9% and a corresponding undershoot of approximately 9%. The size of this over and undershoot does not decrease when increasing the number of Fourier components used, but instead the oscillatory error will become sharper and more concentrated around the discontinuity.

In the context of ocean modeling, the Gibbs phenomenon manifests in finite truncations of spherical harmonic series around coastlines. When computing the spherical harmonic coefficients of an ocean data field, such as the sea surface height, the value of the data field is usually set to 0 over land. While this is physically reasonable, it essentially introduces a jump discontinuity along coastlines, which then adversely affects the convergence of spherical harmonic series.

2.2.1 Cesáro Summation

Cesáro summation is a method for regularizing sums to improve their convergence properties, that can be used to reduce the impact of the Gibbs phenomenon. To perform Cesáro summation, we first create the partial sums

$$S_J = \sum_{n=0}^J \sum_{m=-n}^n \frac{3\rho_w(1+k'_n-h'_n)}{\rho_e(2n+1)} \hat{\eta}_{n,m} Y_n^m(\theta, \phi), \quad (7)$$

before then averaging the partial sums

$$\eta_{\text{SAL}}(\theta, \phi) \approx \frac{1}{N+1} \sum_{n=0}^N S_n, \quad (8)$$

which is equivalent to taking the modified sum

$$\eta_{\text{SAL}}(\theta, \phi) \approx \sum_{n=0}^N \sum_{m=-n}^n \left(1 - \frac{n}{N+1}\right) \frac{3\rho_w(1+k'_n-h'_n)}{\rho_e(2n+1)} \hat{\eta}_{n,m} Y_n^m(\theta, \phi). \quad (9)$$

This can be implemented by modifying the existing spherical harmonic computation with no additional cost. This modification helps to reduce the Gibbs phenomenon along coastlines, but at the same time, it introduces error by acting as a modification on the LLNs.

2.3 Convolutions for Computing SAL

We now describe our alternative to spherical harmonics. The convolution theorem for spherical harmonics (Driscoll and Healy (1994)) states that

$$(\widehat{F * G})_n^m = \sqrt{\frac{4\pi}{2n+1}} \widehat{F}_n^m \widehat{G}_n^0, \quad (10)$$

where F and G are two functions, $F * G$ is the spherical convolution of F and G , \widehat{F}_n^m is the degree n order m spherical harmonic coefficient of F , and likewise for \widehat{G}_n^0 and $(\widehat{F * G})_n^m$. To apply this to SAL, we will take F to be the sea surface height η and G to be an unknown Green's function for the SAL. The convolution of the sea surface height η and G_{SAL} will be the SAL potential η_{SAL} . Thus, $F * G$ will be η_{SAL} . Thus, using Eq. 5, we find that the spherical harmonic coefficients of the Green's function are

$$\widehat{G}_{\text{SAL},n}^0 = \frac{3\rho_w(1+k'_n - h'_n)}{\rho_e \sqrt{4\pi(2n+1)}}, \quad (11)$$

which we sum to give the SAL Green's function as

$$G_{\text{SAL}}(\mathbf{x}, \mathbf{y}) = \sum_{n=0}^{\infty} \frac{3\rho_w(1+k'_n - h'_n)}{4\pi\rho_e} P_n(\mathbf{x} \cdot \mathbf{y}), \quad (12)$$

where P_n is the n -th Legendre polynomial and \mathbf{x} and \mathbf{y} are points on the sphere. With this Green's function, the SAL potential can then be computed as

$$\eta_{\text{SAL}}(\mathbf{x}) = \int_S G_{\text{SAL}}(\mathbf{x} \cdot \mathbf{y}) \eta(\mathbf{y}) dS(\mathbf{y}), \quad (13)$$

where \mathbf{x} and \mathbf{y} are points on the sphere, and $\gamma(\mathbf{x}, \mathbf{y})$ is the great circle angle between the two points, $\arccos(\mathbf{x} \cdot \mathbf{y})$. However, to actually work with Eq. 13, the Green's function cannot be an infinite sum. One idea is to work with a finite truncation, but this is computationally intensive. Instead, we analyze the asymptotic behavior of the LLNs. Working with the LLNs presented in Wang et al. (2012), we empirically determine that

$$k'_n \approx a_1/n, \quad h'_n \approx b_0 + b_1/n, \quad (14)$$

with coefficients $a_1 = -2.7$, $b_0 = -6.21196$, and $b_1 = 6.1$. Using the identities (Gradshteyn and Ryzhik (2014))

$$\sum_{n=0}^{\infty} P_n(x) = \frac{1}{\sqrt{2(1-x)}}, \quad \sum_{n=1}^{\infty} \frac{1}{n} P_n(x) = -\ln(\sqrt{2(1-x)} + 2(1-x)), \quad (15)$$

we can derive a closed form approximation for the Green's function as

$$G_{\text{SAL}}(\mathbf{x}, \mathbf{y}) \approx \frac{3\rho_w}{4\pi\rho_e} \left(\frac{1-b_0}{\sqrt{2-2\mathbf{x} \cdot \mathbf{y}}} - (a_1 - b_1) \ln \left(\sqrt{2-2\mathbf{x} \cdot \mathbf{y}} + 2 - 2\mathbf{x} \cdot \mathbf{y} \right) \right), \quad (16)$$

However, this is not yet the final form of the Green's function. Looking at Eq. 3, what we need is the gradient of the SAL. Taking the gradient, we have that

$$\nabla \eta_{\text{SAL}}(\mathbf{x}) = \int_S \nabla(G_{\text{SAL}}(\gamma(\mathbf{x}, \mathbf{y}))) \eta(\mathbf{y}) dS(\mathbf{y}), \quad (17)$$

with the horizontal gradient falling on the \mathbf{x} variable of the Green's function in the integral. Using the chain rule, the gradient of the Green's function is then

$$\nabla G_{\text{SAL}}(\mathbf{x} \cdot \mathbf{y}) = \frac{dg_{\text{SAL}}(\gamma)}{d \cos \gamma} \nabla \cos \gamma(\mathbf{x}, \mathbf{y}), \quad (18)$$

where $\gamma(\mathbf{x}, \mathbf{y})$ is the great circle angle between \mathbf{x} and \mathbf{y} . Taking these derivatives, we find the integral kernel for the SAL gradient is

$$\nabla G_{\text{SAL}}(\mathbf{x}, \mathbf{y}) = \frac{3\rho_w}{4\pi\rho_e R_E} \begin{bmatrix} y_3(1-x_3^2) - x_3(x_1y_1 + x_2y_2) \\ x_1y_2 - x_2y_1 \end{bmatrix} \left(\frac{b_1 - 1}{(2 - 2\mathbf{x} \cdot \mathbf{y})^{3/2}} + \frac{(a_1 - b_1)(2 - 2\mathbf{x} \cdot \mathbf{y} + \sqrt{2 - 2\mathbf{x} \cdot \mathbf{y}})}{2((\mathbf{x} \cdot \mathbf{y})^2 - 1)} \right), \quad (19)$$

where (x_1, x_2, x_3) are the Cartesian components of \mathbf{x} , and (y_1, y_2, y_3) are the Cartesian components of \mathbf{y} . This is no longer a Green's function as it is not symmetric in \mathbf{x} and \mathbf{y} .

2.3.1 Fast Summation for Accelerating Convolutions

To discretize Eq. 17, we use the midpoint rule. For a set of N grid points $\{\mathbf{x}_i\}$, the discretized integral is approximated as

$$\nabla \eta_{\text{SAL}}(\mathbf{x}_i) = \sum_{j=1, j \neq i}^N \nabla g_{\text{SAL}}(\mathbf{x}_i, \mathbf{x}_j) \eta(\mathbf{x}_j) A_j, \quad i = 1, \dots, N, \quad (20)$$

where A_j is the area associated with grid point \mathbf{x}_j . First, we note that when discretized, the sum is singular when $i = j$. To remedy this, we skip the singularity by omitting $i = j$ from the sum. Second, we note that this sum scales like $O(N^2)$, which is prohibitive for scaling to high resolutions. We use fast summation to avoid this issue. Fast summation refers to a family of techniques for approximating such sums in $O(N \log N)$ or $O(N)$ time complexity. For this, we use the Cubed Sphere Fast Multipole Method (CSFMM) presented in Chen and Krasny (2025). The CSFMM is based on the use of barycentric Lagrange interpolation with proxy points defined by the tensor product Chebyshev points in a cubed sphere tree structure, allows for the computation of the discretized integral in $O(N)$ computation. The cubed sphere tree structure is used to divide points into clusters, and when a cluster has many points, barycentric Lagrange interpolation is then used to perform approximations to reduce the amount of computation. This introduces a small and controllable amount of error. The use of the tree structure naturally adapts to the irregular distribution of ocean grid points around coastlines, and this method additionally operates entirely on the sphere and not in 3d Cartesian space, as with many other methods.

3 Simulation Details

We implement this convolution and CSFMM in MOM6. To evaluate the convolution method for computing SAL, we run MOM6 and force the model with the M_2 tide. The model is initialized with zero velocity initial conditions, and is run for 20

days with a time step of $\Delta t = 180$ s. The last three days of model output are used for the error computation. We test with two different grid spacings: one with nominal spacing of 0.36 degrees (a grid spacing typical of low-resolution climate change simulations), and one with nominal spacing of 0.08 degrees (a grid spacing typical for higher-resolution simulations usually run over shorter durations than climate change simulations). We use a single level configuration. The SAL term is computed at every time step. The model was run on Derecho (Computational and Information Systems Laboratory (2023)). We use a topography and wave drag based on GEBCO 2008, as used in Wang et al. (2024). For the grid with 0.36 degree nominal grid spacing, we use several different SAL configurations. We use the spherical harmonic SAL with $n = 40$ spherical harmonic components, the standard configuration, as well as $n = 200$ spherical harmonic components, to test the convergence. We also test the Cesàro modified spherical harmonic SAL with $n = 40$, $n = 200$, and $n = 400$ spherical harmonic components. Lastly, we test the convolution SAL as well. For the grid with 0.08 degree nominal grid spacing, we test only the standard spherical harmonic SAL with $n = 40$ and $n = 200$ spherical harmonic components and the convolution SAL.

3.0.1 Measuring Error

To measure the error in the model tides, we compare the model output with the TPXO9 dataset (Erofeeva and Egbert (2018)), which comes from a hydrodynamical model that assimilates satellite observations of tidal sea surface heights. To do this, we first compute

$$D^2 = \frac{1}{2}(A_{\text{TPXO}}^2 - A_{\text{MOM6}}^2) - A_{\text{TPXO}} A_{\text{MOM6}} \cos(\varphi_{\text{TPXO}} - \varphi_{\text{MOM6}}), \quad (21)$$

at each grid point, where A is the amplitude of the tidal constituent and φ is the Greenwich phase lag. The error is then computed as

$$\text{RMSE} = \left(\frac{1}{4\pi R_E^2} \int_S D^2 dS \right)^{1/2}, \quad (22)$$

We can also decompose the RMSE into an amplitude error and a phase error. Additionally, we compute the error for both the entire ocean, and for the grid points between 66 degrees south and 66 degrees north that have a depth of greater than 1000 meters in order to filter out the impact from coastal topography and limited satellite altimetry coverage in polar areas.

3.0.2 Tuning

The parameter χ in the wave drag scheme is tuned for each method of computing the SAL. The tuning is performed in order to minimize the $RMSE$, but one can understand the need for tuning using energy arguments (Arbic et al. (2004)). If χ is too large, then too much energy will be dissipated, and if χ is not large enough, then not enough energy will be dissipated. Both extremes above will adversely affect the accuracy of the modeled tides. The different ways of computing the SAL will result in accelerations of different magnitudes, and as a result, χ must change accordingly. The χ parameters that are used are presented in Table 1.

0.36 degree nominal grid spacing	Wave drag χ	Deep non-polar ocean			Global ocean		
		Total RMSE	Amplitude error	Phase error	Total RMSE	Amplitude error	Phase error
Spherical harmonic SAL, $n = 40$	1.0	8.10	4.35	6.80	10.20	6.25	8.06
Spherical harmonic SAL, $n = 200$	1.0	8.07	4.34	6.78	10.17	6.24	8.02
Cesáro SH SAL, $n = 40$	1.0	9.63	4.85	8.31	11.69	6.66	9.60
Cesáro SH SAL, $n = 200$	1.0	8.36	4.43	7.09	10.46	6.32	8.33
Cesáro SH SAL, $n = 400$	1.0	8.21	4.38	6.94	10.32	6.29	8.18
Convolution SAL	0.7	5.82	3.89	4.33	8.34	5.93	5.86

Table 1. Wave drag tuning parameter χ and errors for different methods of computing SAL for 0.36 degree nominal grid spacing.

0.08 degree nominal grid spacing	Wave drag χ	Deep non-polar ocean			Global ocean		
		Total RMSE	Amplitude error	Phase error	Total RMSE	Amplitude error	Phase error
Spherical harmonic SAL, $n = 40$	0.8	3.99	2.32	3.25	6.68	4.72	4.72
Spherical harmonic SAL, $n = 200$	0.8	4.00	2.32	3.26	6.71	4.73	4.75
Convolution SAL	0.5	3.64	2.00	3.06	5.93	4.11	4.30

Table 2. As in Tbl. 1, but with 0.08 degree nominal grid spacing.

4 Results

4.1 TPXO9 Comparison

We present our error results in Table 1 and 2. Denoting the maximum degree of spherical harmonics used as n , we compare the spherical harmonic SAL with a Cesáro modified spherical harmonic SAL, as well as the convolution SAL. On a mesh with 0.36 degree nominal grid spacing, the spherical harmonic SAL with $n = 40$ results in a deep non-polar RMSE of 8.10 cm, with the phase error contributing 6.80 cm of this error. The global RMSE of 10.20 cm is similarly dominated by the phase error of 8.06 cm. The spherical harmonic SAL run with $n = 200$ has a similar RMSE of 8.07 cm in the deep non-polar ocean and 10.17 cm in the entire ocean. With the Cesáro modified spherical harmonic SAL runs, we observe larger errors than when the standard spherical harmonic SAL is used. However, as we increase the number of spherical harmonic components used for the Cesáro spherical harmonic SAL, we observe a reduction in the error as we go from $n = 40$ to $n = 200$ and $n = 400$. With the convolution SAL computation, we reduce the RMSE considerably from 8.10 cm to 5.82 cm, with most of the improvement coming from a reduction in the phase error, from 6.80 cm to 4.33 cm. Likewise, in the global ocean, we reduce the phase error from 8.06 cm to 5.86 cm. With the runs at 0.08 degree nominal grid spacing, we observe a significant reduction in error compared to the model runs at 0.36 degree nominal grid spacing. However, there are differences in the error behavior. First, using up to $n = 200$ degree spherical harmonics increases the error slightly, compared to using only up to $n = 40$. Additionally, in contrast to the results with 0.36 degree nominal grid spacing, in the higher resolution 0.08 degree grid spacing results, the convolution SAL does not present as large of an error improvement compared to the spherical harmonic SAL.

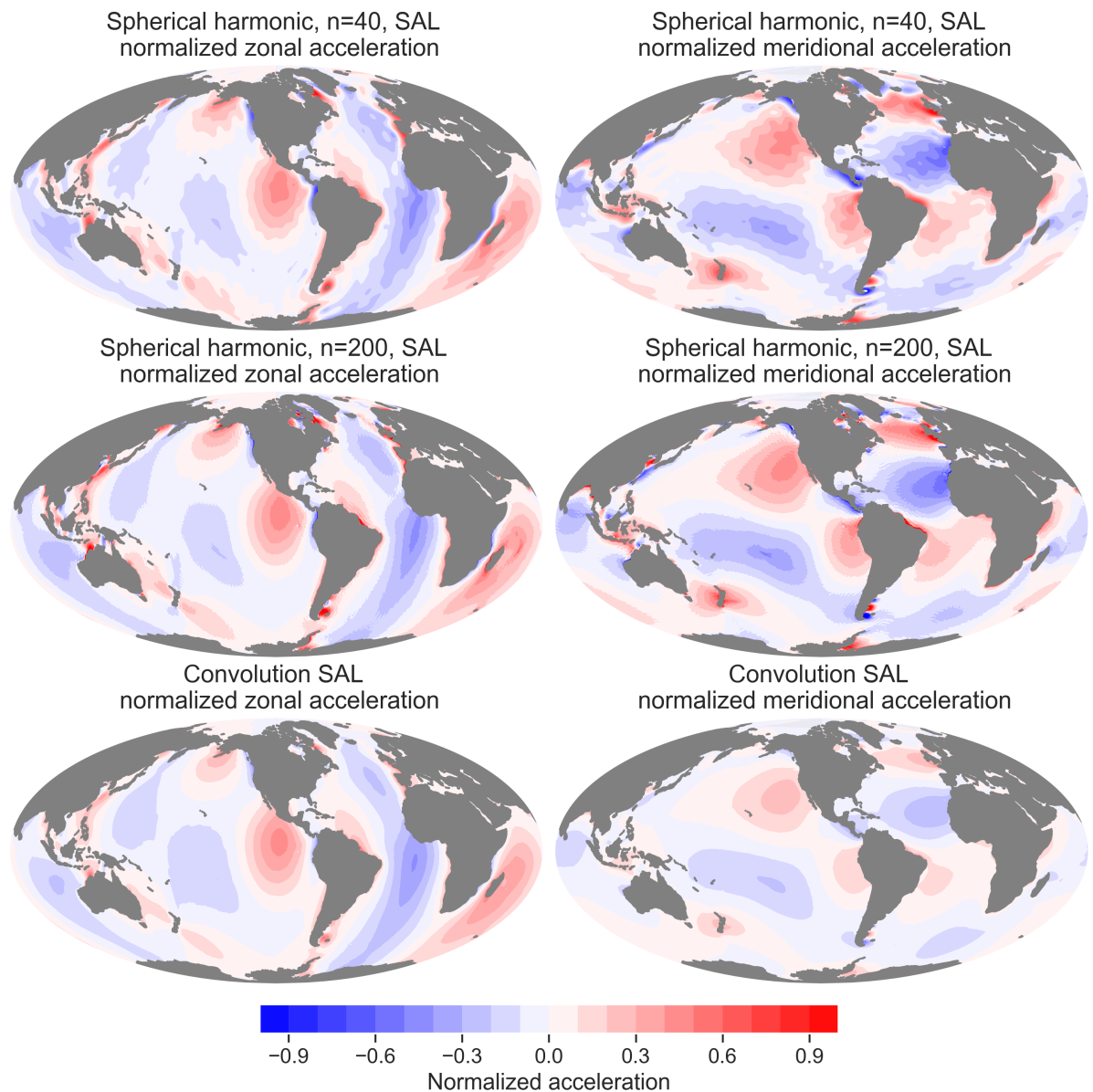


Figure 1. SAL acceleration computed from spherical harmonic and convolution based SAL techniques. The accelerations are normalized by dividing the largest magnitude of acceleration.

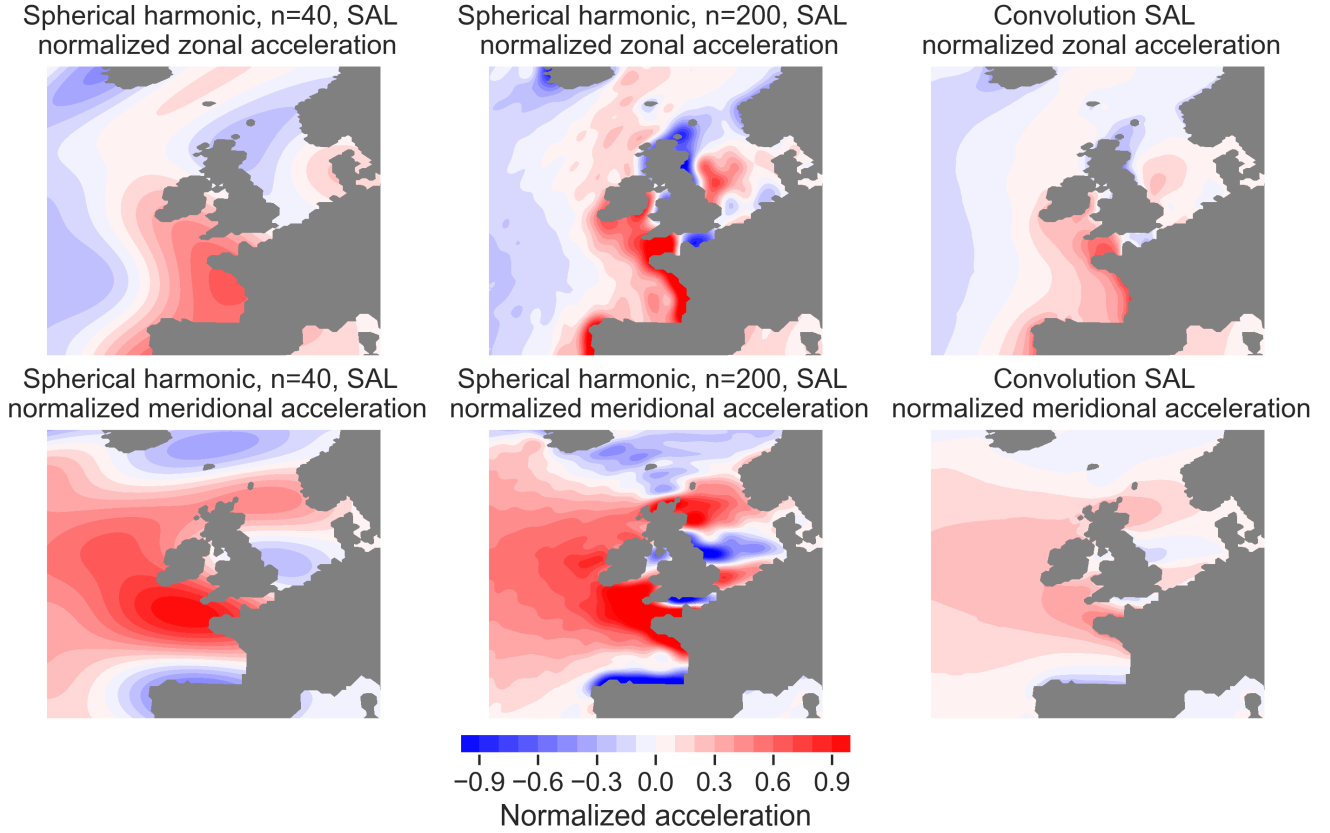


Figure 2. As in Fig. 1, but focused on the Northeast Atlantic and North Sea.

The question arises: what is the reason for the improvement in the results that use a convolution SAL, especially the improvement in the tidal phase? To address this, we examine the corresponding SAL acceleration, $g\nabla\eta_{\text{SAL}}$, focusing on the spherical harmonic and convolution based SAL fields. The zonal and meridional acceleration for the spherical harmonic and convolution accelerations at a single time step display significant differences (Fig. 1). The overall structure of the acceleration is the same in the spherical harmonic and convolution computations. However, the spherical harmonic computation with degree $n = 40$ exhibits a large number of small oscillations, arising from the truncation of the spherical harmonic series. The spherical harmonic computation with degree $n = 200$ has a similar structure as the computation with $n = 40$, but without the oscillations. However, with $n = 200$, the error has not significantly reduced, so these small oscillations in the open ocean cannot explain the differences in the error between $n = 40$ and $n = 200$ simulations. There are large spurious coastal accelerations in both spherical harmonic calculations, as a result of the Gibbs phenomenon. In contrast, with the convolution based SAL, the large spurious coastal accelerations are removed.

This removal of the Gibbs phenomenon is especially apparent in zoomed-in views of coastal regions (Fig. 2). Using the Northeast Atlantic and North Sea regions as examples, we see a significant difference in the spatial structure of the acceleration

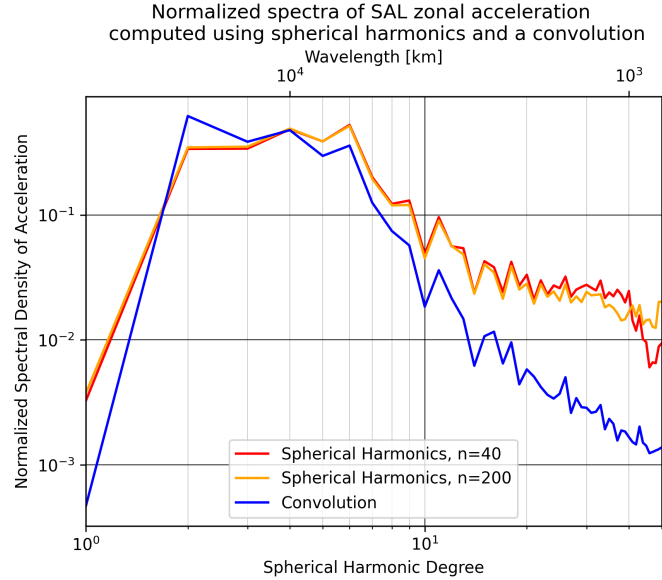


Figure 3. Spherical harmonic spectra of the SAL acceleration, computed from the zonal accelerations in Fig. 1 over the ocean grid points. The spectra are normalized to unit norm. The wavelength for a given spherical harmonic degree is $2\pi R_E/n$.

when we go from $n = 40$ to $n = 200$ spherical harmonic components. In contrast, with the convolution, we have a similar spatial structure to the spherical harmonic computation with $n = 200$, showing that we resolve fine scales, but the amplitude of the acceleration is smaller, as we have removed the Gibbs errors. The adverse impact of the Gibbs phenomenon also explains why using $n = 200$ spherical harmonics instead of $n = 40$ spherical harmonics has a minimal impact on the tidal errors. Increasing the number of spherical harmonics used does not decrease the magnitude of the Gibbs error near the coastlines. Instead, with more spherical harmonics, the oscillations become more concentrated along the coastlines, and when the gradient is taken with $n = 200$, the accelerations are also larger.

Another question arises—why does the removal of the Gibbs error in coastal regions yield an improvement in the error observed in the deep, non-polar ocean? We speculate that the reason for the global improvement in the tides is due to the “back effect” of regions of large resonant coastal tides upon open-ocean tides (Arbic et al. (2007, 2009); Arbic and Garrett (2010)). Changes to the tides in small coastal regions, especially those regions with large resonant coastal tides, can have a large back effect on the global tides. Thus, it appears that the improvements to the SAL in coastal regions as a result of using the convolution SAL can drive improvements in the tides in the entire ocean. Further mechanistic exploration into the role of the back effect in the results shown here is left as a topic for future work.

The wavenumber spectra of the acceleration (Fig. 3) also reveals illuminating differences. While the spherical harmonic and convolution SAL have similar accelerations at low wavenumbers, at higher wave numbers, the spectra for the convolution SAL acceleration drops off much faster than it does for the spherical harmonic SAL acceleration. As a result, we can say that the convolution SAL produces a smoother acceleration. The convolution based SAL is smoother than the spherical harmonic

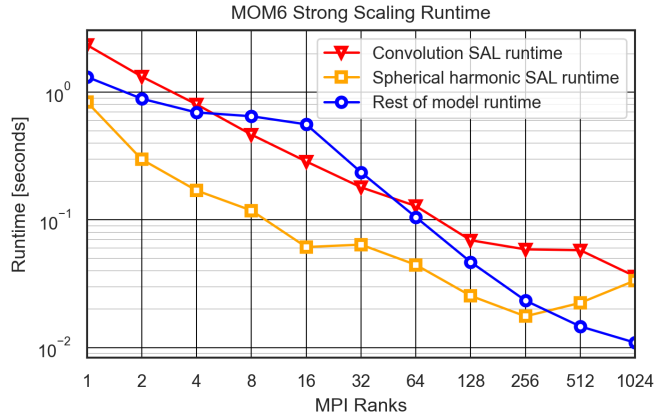


Figure 4. Strong scaling of the two methods of computing SAL at 0.36 degree nominal grid spacing.

SAL for two reasons. First, the convolution based SAL does not suffer from Gibbs errors near the coastlines. In setting the sea surface height η to 0 over land, discontinuities are introduced, and any finite truncation of the spherical harmonics will have Gibbs errors. In contrast, the convolution incorporates behavior at all wavenumbers and thus, avoids finite truncation problems. Secondly, MOM6 uses a staggered C-grid. The spherical harmonic SAL computes the SAL potential at cell centers, and then uses finite differences to compute the accelerations at the cell edges. In contrast, the convolution SAL computes the SAL acceleration at the cell center, and then averages to compute the acceleration at the cell edges. The finite difference amplifies small scales, while the averaging serves to smooth them.

4.2 Runtime Performance

We perform a strong scaling analysis to verify that the convolution based SAL computation does not have an excessive runtime impact. Using MOM6’s internal performance analysis tools, we record the time needed for a single time step while varying the number of MPI ranks from 1 to 1024. The single time step runtime is displayed in Fig. 4. While the spherical harmonic computation is less expensive, it does not parallelize as well as the convolution computation, and at 1024 MPI ranks, the two methods have a similar runtime impact. The runtime impact from this SAL calculation is on the order of 1 or 2 model levels. While this impact is considerable for a single layer simulation, for a multi-layer simulation, the runtime impact will be correspondingly much smaller.

5 Conclusions

Tides are an important component of the Earth system. In the numerical modeling of tides, capturing the effects of SAL is important for accurate simulations. Many ocean tide models employ spherical harmonics to compute SAL. In this work, we present an alternative method of computing SAL, based on a spherical convolution which we accelerate with a fast multipole

method. We implemented this computation in the ocean model MOM6 and ran a number of tidal simulations to validate the computation, comparing the results with the TPXO9 tidal atlas. The tidal error results compare favorably to results employing the spherical harmonic SAL that is currently used, and the runtime impact is not prohibitive.

In this work, we focused on global ocean models. However, regional ocean models are also of great importance, and incorporating the tides and SAL in regional ocean models is also a topic of interest (Irazoqui Apecechea et al. (2017)). Spherical harmonic SAL based techniques cannot be used in such regional models due to the inherently global nature of spherical harmonics. In the future, we plan on exploring the use of the convolution SAL in regional models.

Additionally, there remains work to be done in the physical accuracy of the computed SAL. The approximations used in the derivation of this SAL Green’s function introduce some error. Furthermore, there are physical effects which are not yet incorporated. The interior of the Earth is not homogeneous and the loading response to the ocean tide will vary spatially (Pagiatakis (1990); Scherneck (1991)). The loading response is also not instant, and propagates at some finite speed (Ghobadi-Far et al. (2019)). These effects are difficult to incorporate with spherical harmonics. However, a spatially varying Green’s function could incorporate the Earth’s interior inhomogeneity, and various applications of convolutions already use Green’s functions with time delay incorporated.

Code and data availability. The current version of MOM6 is available from <https://github.com/noaa-gfdl/MOM6> under the GNU Lesser General Public License. The exact version of the model used to produce the results used in this paper is archived on repository under DOI 10.5281/zenodo.18445619 (Chen and Wang (2026)), as are input data and scripts to run the model and produce the plots for all the simulations presented in this paper.

Author contributions. BKA and RK conceptualized the project. AC conducted the formal analysis and investigation. AC and HW produced the software. HW provided datasets. BKA and RK supervised the project. AC visualized the results and prepared the original draft. HW, BKA, and RK assisted in reviewing and editing the manuscript.

Competing interests. The authors declare that they have no conflict of interest.

Acknowledgements. AC is supported by the National Science Foundation Graduate Research Fellowship Program under Grant Number DGE 2241144. Any opinions, findings, and conclusions or recommendations expressed in this material are those of the authors and do not necessarily reflect the views of the National Science Foundation. BKA is grateful for sabbatical support from the Australian National University, especially Callum Shakespeare, Andy Hogg, and Adele Morrison, during the 2024–2025 academic year. BKA acknowledges support from Office of Naval Research grant N00017-22-1-2576. The authors thank Robert Hallberg (National Oceanic and Atmospheric Administration, Geophysical Fluid Dynamics Laboratory) and Alan Wallcraft (Florida State University) for useful discussions.

References

Accad, Y. and Pekeris, C. L.: Solution of the tidal equations for the M2 and S2 tides in the world oceans from a knowledge of the tidal potential alone, *Philos. Trans. R. Soc. London, Ser. A*, 290, 235–266, 1978.

Adcroft, A., Anderson, W., Balaji, V., Blanton, C., Bushuk, M., Dufour, C. O., Dunne, J. P., Griffies, S. M., Hallberg, R., Harrison, M. J., et al.: The GFDL global ocean and sea ice model OM4. 0: Model description and simulation features, *J. Adv. Model. Earth Syst.*, 11, 3167–3211, 2019.

Arbic, B. K.: Incorporating tides and internal gravity waves within global ocean general circulation models: A review, *Prog. Oceanogr.*, 206, 102 824, 2022.

Arbic, B. K. and Garrett, C.: A coupled oscillator model of shelf and ocean tides, *Cont. Shelf Res.*, 30, 564–574, 2010.

Arbic, B. K., Garner, S. T., Hallberg, R. W., and Simmons, H. L.: The accuracy of surface elevations in forward global barotropic and baroclinic tide models, *Deep Sea Res. Part II*, 51, 3069–3101, 2004.

Arbic, B. K., St-Laurent, P., Sutherland, G., and Garrett, C.: On the resonance and influence of the tides in Ungava Bay and Hudson Strait, *Geophys. Res. Lett.*, 34, 2007.

Arbic, B. K., Karsten, R. H., and Garrett, C.: On tidal resonance in the global ocean and the back-effect of coastal tides upon open-ocean tides, *Atmos. Ocean*, 47, 239–266, 2009.

Arbic, B. K., Wallcraft, A. J., and Metzger, E. J.: Concurrent simulation of the eddying general circulation and tides in a global ocean model, *Ocean Modell.*, 32, 175–187, 2010.

Barton, K. N., Pal, N., Brus, S. R., Petersen, M. R., Arbic, B. K., Engwirda, D., Roberts, A. F., Westerink, J. J., Wirasaet, D., and Schindelegger, M.: Global barotropic tide modeling using inline self-attraction and loading in MPAS-Ocean, *J. Adv. Model. Earth Syst.*, 14, e2022MS003 207, 2022.

Brus, S. R., Barton, K. N., Pal, N., Roberts, A. F., Engwirda, D., Petersen, M. R., Arbic, B. K., Wirasaet, D., Westerink, J. J., and Schindelegger, M.: Scalable self attraction and loading calculations for unstructured ocean tide models, *Ocean Modell.*, 182, 102 160, 2023.

Buijsman, M. C., Arbic, B. K., Green, J., Helber, R. W., Richman, J. G., Shriver, J. F., Timko, P., and Wallcraft, A.: Optimizing internal wave drag in a forward barotropic model with semidiurnal tides, *Ocean Modell.*, 85, 42–55, 2015.

Chen, A. and Krasny, R.: A Cubed Sphere Fast Multipole Method, *arXiv preprint arXiv:2508.13550*, 2025.

Chen, A. and Wang, H.: Convolution Based Self Attraction and Loading in MOM6, <https://doi.org/10.5281/zenodo.18445619>, 2026.

Computational and Information Systems Laboratory : Derecho: HPE Cray EX System (University Community Computing), NSF: National Center for Atmospheric Research , Boulder, CO, doi:10.5065/qx9a-pg09, 2023.

Cummins, P. F. and Oey, L.-Y.: Simulation of barotropic and baroclinic tides off northern British Columbia, *J. Phys. Oceanogr.*, 27, 762–781, 1997.

Driscoll, J. R. and Healy, D. M.: Computing Fourier transforms and convolutions on the 2-sphere, *Adv. Appl. Math.*, 15, 202–250, 1994.

Egbert, G. D., Bennett, A. F., and Foreman, M. G.: TOPEX/POSEIDON tides estimated using a global inverse model, *J. Geophys. Res.: Oceans*, 99, 24 821–24 852, 1994.

Erofeeva, S. and Egbert, G. D.: TPXO9-a new global tidal model in TPXO series, in: American Geophysical Union, Ocean Sciences Meeting, 186, pp. PL34C–186, 2018.

Farrell, W.: Deformation of the Earth by surface loads, *Rev. Geophys.*, 10, 761–797, 1972.

Ghobadi-Far, K., Han, S.-C., Sauber, J., Lemoine, F., Behzadpour, S., Mayer-Gürr, T., Sneeuw, N., and Okal, E.: Gravitational changes of the Earth's free oscillation from earthquakes: Theory and feasibility study using GRACE inter-satellite tracking, *J. Geophys. Res.: Solid Earth*, 124, 7483–7503, 2019.

Gordeev, R., Kagan, B., and Polyakov, E.: The effects of loading and self-attraction on global ocean tides: The model and the results of a numerical experiment, *J. Phys. Oceanogr.*, 7, 161–170, 1977.

Gottlieb, D. and Shu, C.-W.: On the Gibbs phenomenon and its resolution, *SIAM Rev.*, 39, 644–668, 1997.

Gradshteyn, I. S. and Ryzhik, I. M.: Table of integrals, series, and products, Academic press, 2014.

Hendershott, M.: The effects of solid Earth deformation on global ocean tides, *Geophys. J. Int.*, 29, 389–402, 1972.

Irazoqui Apecechea, M., Verlaan, M., Zijl, F., Le Coz, C., and Kernkamp, H.: Effects of self-attraction and loading at a regional scale: a test case for the Northwest European Shelf, *Ocean Dyn.*, 67, 729–749, 2017.

Jayne, S. R. and St. Laurent, L. C.: Parameterizing tidal dissipation over rough topography, *Geophys. Res. Lett.*, 28, 811–814, 2001.

Kang, S. K., Foreman, M. G., Lie, H.-J., Lee, J.-H., Cherniawsky, J., and Yum, K.-D.: Two-layer tidal modeling of the Yellow and East China Seas with application to seasonal variability of the M2 tide, *J. Geophys. Res.: Oceans*, 107, 6–1, 2002.

Le Provost, C., Genco, M., Lyard, F., Vincent, P., and Caneil, P.: Spectroscopy of the world ocean tides from a finite element hydrodynamic model, *J. Geophys. Res.: Oceans*, 99, 24 777–24 797, 1994.

Merrifield, M. A., Holloway, P. E., and Johnston, T. S.: The generation of internal tides at the Hawaiian Ridge, *Geophys. Res. Lett.*, 28, 559–562, 2001.

Müller, M., Haak, H., Jungclaus, J. H., Sündermann, J., and Thomas, M.: The effect of ocean tides on a climate model simulation, *Ocean Modell.*, 35, 304–313, 2010.

Munk, W. and Wunsch, C.: Abyssal recipes II: Energetics of tidal and wind mixing, *Deep Sea Res. Part I*, 45, 1977–2010, 1998.

Pagiatakis, S. D.: The response of a realistic Earth to ocean tide loading, *Geophys. J. Int.*, 103, 541–560, 1990.

Parke, M. E. and Hendershott, M. C.: M2, S2, K1 models of the global ocean tide on an elastic Earth, *Mar. Geod.*, 3, 379–408, 1980.

Ray, R.: Ocean self-attraction and loading in numerical tidal models, *Mar. Geod.*, 21, 181–192, 1998.

Ray, R. D.: Global ocean tide models on the eve of TOPEX/POSEIDON, *IEEE Trans. Geosci. Remote Sens.*, 31, 355–364, 1993.

Scherneck, H.-G.: A parametrized solid Earth tide model and ocean tide loading effects for global geodetic baseline measurements, *Geophys. J. Int.*, 106, 677–694, 1991.

Schiller, A. and Fiedler, R.: Explicit tidal forcing in an ocean general circulation model, *Geophys. Res. Lett.*, 34, 2007.

Schwiderski, E.: Global Ocean Tides: The semidiurnal principal lunar tide (M2), atlas of tidal charts and maps, Naval Surface Weapons Center, 1979.

Shum, C., Woodworth, P., Andersen, O., Egbert, G. D., Francis, O., King, C., Klosko, S., Le Provost, C., Li, X., Molines, J.-M., et al.: Accuracy assessment of recent ocean tide models, *J. Geophys. Res.: Oceans*, 102, 25 173–25 194, 1997.

Simpson, J. H. and Hunter, J.: Fronts in the Irish sea, *Nature*, 250, 404–406, 1974.

Stammer, D., Ray, R. D., Andersen, O. B., Arbic, B. K., Bosch, W., Carrere, L., Cheng, Y., Chinn, D. S., Dushaw, B. D., Egbert, G. D., et al.: Accuracy assessment of global barotropic ocean tide models, *Rev. Geophys.*, 52, 243–282, 2014.

Stepanov, V. N. and Hughes, C. W.: Parameterization of ocean self-attraction and loading in numerical models of the ocean circulation, *J. Geophys. Res.: Oceans*, 109, 2004.

Thomas, M., Sündermann, J., and Maier-Reimer, E.: Consideration of ocean tides in an OGCM and impacts on subseasonal to decadal polar motion excitation, *Geophys. Res. Lett.*, 28, 2457–2460, 2001.

Wang, H., Xiang, L., Jia, L., Jiang, L., Wang, Z., Hu, B., and Gao, P.: Load Love numbers and Green's functions for elastic Earth models PREM, iasp91, ak135, and modified models with refined crustal structure from Crust 2.0, *Comput. Geosci.*, 49, 190–199, 2012.

Wang, H., Hallberg, R., Wallcraft, A. J., Arbic, B. K., and Chassignet, E. P.: Improving global barotropic tides with sub-grid scale topography, *J. Adv. Model. Earth Syst.*, 16, e2023MS004 056, 2024.

Waterhouse, A. F., MacKinnon, J. A., Nash, J. D., Alford, M. H., Kunze, E., Simmons, H. L., Polzin, K. L., St. Laurent, L. C., Sun, O. M., Pinkel, R., et al.: Global patterns of diapycnal mixing from measurements of the turbulent dissipation rate, *J. Phys. Oceanogr.*, 44, 1854–1872, 2014.